



Cite this: *J. Mater. Chem. C*, 2020, 8, 5769

tert-Butyl substituted hetero-donor TADF compounds for efficient solution-processed non-doped blue OLEDs†

Feng-Ming Xie,^{‡a} Zhi-Dong An,^{‡a} Miao Xie,^a Yan-Qing Li,^{*ab} Guang-Hui Zhang,^a Shi-Jie Zou,^a Li Chen,^a Jing-De Chen,^a Tao Cheng^{id} ^{*a} and Jian-Xin Tang^{id} ^{*ac}

For the development of solution-processed organic light-emitting diodes (OLEDs), it is highly desirable yet challenging to realize solution-processable non-doped thermally activated delayed fluorescence (TADF) emitters due to their high efficiency and excellent compatibility to the wet methods. Herein, two pairs of blue TADF isomers are designed and synthesized with a hetero-donor configuration for the realization of high photoluminescent quantum yield. The incorporation of two *tert*-butyl groups in the molecules can effectively increase the molecular solubility and reduce the aggregation-caused self-quenching of excitons in neat films by inhibiting the intramolecular vibrational relaxation and the intermolecular π - π stacking. Solution-processed non-doped OLEDs are achieved with these blue TADF emitters, exhibiting the record-high external quantum efficiencies (EQE) of 25.8%. Furthermore, an all-TADF white OLED with an EQE of 27.3% is also achieved by employing a single emitting layer with the blue TADF emitter as a host for an orange-red TADF dopant.

Received 12th February 2020,
Accepted 16th March 2020

DOI: 10.1039/d0tc00718h

rsc.li/materials-c

1. Introduction

Solution-processed organic light-emitting diodes (OLEDs) have recently attracted tremendous attention for display and lighting applications due to some unique advantages over the conventional vacuum deposition, such as excellent compatibility to low-cost and easily scalable manufacturing, relatively small amounts of wasted materials, and precise control over the doping concentration in co-doping host-guest systems.^{1–6} To realize solution-processed OLEDs with good performance, several requirements should be satisfied for the emitting materials, including efficient luminance, good solubility, high thermal stability, and good film formation ability

during the solution process.^{1,7} However, the development of high-performance solution-processable emitters is still technically challenging, since the conventional fluorescent emitters are limited by poor 25% internal quantum efficiency (IQE) while phosphorescent emitters suffer from the use of expensive noble-metal elements (*e.g.*, Ir, Pt or Au). Emerging as a new-generation class of emitters,^{8–13} all-organic thermally activated delayed fluorescence (TADF) materials offer a promising alternative to conventional fluorescence and phosphorescent emitters due to the intrinsic merit of theoretical 100% exciton harvesting capability for both singlet (S_1) and triplet (T_1) excitons through efficient reverse intersystem crossing (RISC) process.

In spite of the great progress in highly efficient TADF materials, state-of-the-art solution-processed OLEDs using TADF emitters, especially non-doped emitting layers, are very rare.^{14–20} In particular, most of the blue TADF emitters reported so far suffer from aggregation-caused quenching (ACQ) in neat films, which have to be used in the co-doping systems with precise control of the doping concentration.^{21–23} As a result, the choices of suitable host materials are critical for blue TADF emitters and the preparation of the emitting layers is rather complicated in solution-processed OLEDs. There is thus an urgent demand to realize solution-processable blue TADF emitters with high light-emitting efficiency and negligible concentration quenching in solution-processed non-doped films. One general strategy to obtain efficient blue TADF emitters is to introduce a largely twisted donor-acceptor configuration with a phenyl linker, in which small singlet-triplet energy

^a Jiangsu Key Laboratory for Carbon-Based Functional Materials & Devices, Institute of Functional Nano & Soft Materials (FUNSOM), Soochow University, Suzhou, Jiangsu 215123, China. E-mail: yqli@suda.edu.cn, tcheng@suda.edu.cn, jxtang@suda.edu.cn

^b School of Physics and Electronics Science, Ministry of Education Nanophotonics & Advanced Instrument Engineering Research Center, East China Normal University, Shanghai, 200062, China

^c Institute of Organic Optoelectronics (IOO), JITRI, Wujiang, Suzhou 215215, China

† Electronic supplementary information (ESI) available: Experimental details including general information, synthesis procedure and photophysical properties as well as device fabrication and characterization, single-crystal structures, the TGA and DSC thermograms, PL spectra in different solvents, CV curves, temperature-dependent transient PL decay curves, natural transition orbital analysis, AFM images and the performances of the devices. See DOI: 10.1039/d0tc00718h

‡ These authors contribute equally to this work.

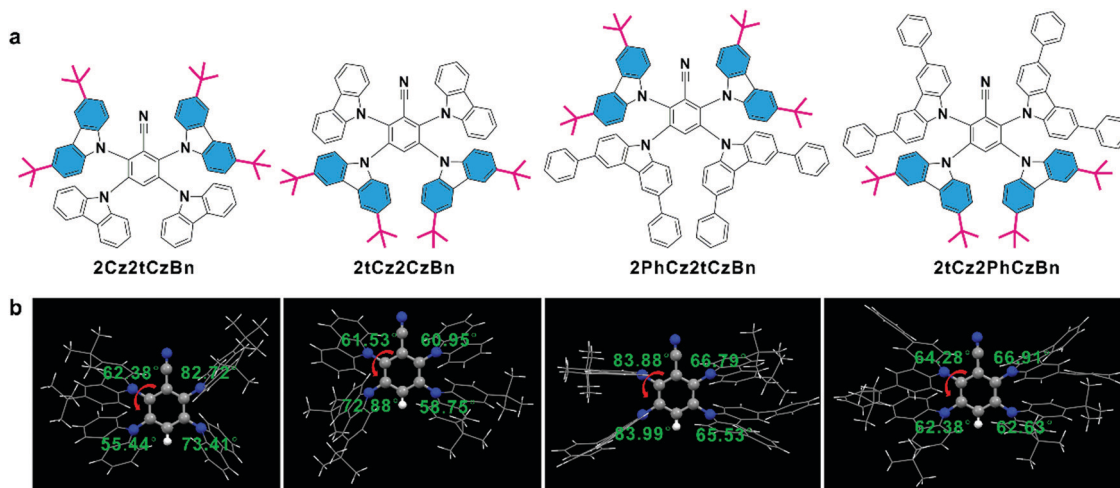


Fig. 1 (a) Chemical structures and (b) crystal structures and selected twisted angles of **2Cz2tCzBn**, **2tCz2CzBn**, **2PhCz2tCzBn**, and **2tCz2PhCzBn**.

splitting (ΔE_{ST}) can be achieved by separating the highest occupied molecular orbital (HOMO) and the lowest unoccupied molecular orbital (LUMO).^{24–26} Meanwhile, the construction of non-planar structures with highly twisted moieties can efficiently suppress the concentration quenching of non-doped TADF materials.^{27,28} In addition, the utilization of alkyl substituents such as *tert*-butyl and adamantyl can improve the molecular solubility and film formation ability of TADF emitters.^{7,29,30}

Herein, two pairs of isomer solution-processable blue TADF emitters (Fig. 1a), namely **2Cz2tCzBn**, **2tCz2CzBn**, **2PhCz2tCzBn**, and **2tCz2PhCzBn**, respectively, are designed with a hetero-donor configuration, featuring cyanobenzene as an acceptor core, and 3,6-ditertbutylcarbazole as a second donor unit as compared to the initial single donor (carbazole or 3,6-diphenylcarbazole) for the realization of small ΔE_{ST} and high photoluminescent quantum yield (PLQY).³¹ The incorporation of two *tert*-butyl groups in the molecules can effectively increase the molecular solubility and reduce the ACQ by inhibiting the intramolecular vibrational relaxation and the intermolecular π - π stacking. Solution-processed non-doped OLEDs are achieved with these blue TADF emitters, exhibiting external quantum efficiencies (EQEs) of 25.8%, 24.5%, 19.5%, and 19.1% for **2Cz2tCzBn**, **2tCz2CzBn**, **2PhCz2tCzBn**, and **2tCz2PhCzBn**, respectively. More fascinatingly, high-performance solution-processed white OLEDs are realized by employing a single-emitting layer with the blue TADF emitter as a host matrix for an orange-red TADF dopant, 3DMAC-BP.³² By optimizing the doping concentration of 3DMAC-BP, the white device shows an EQE of 27.3% and a current efficiency of 67.0 cd A⁻¹. These results validate the potential applications of these solution-processable blue TADF emitters in versatile device architectures.

2. Results and discussion

2.1. Synthesis and single-crystal structures

The synthetic procedures and characterizations of **2Cz2tCzBn**, **2tCz2CzBn**, **2PhCz2tCzBn** and **2tCz2PhCzBn** are described in

detail in Scheme S1 and Fig. S1–S9 (ESI†). All the emitters show excellent solubility in the common solvents, such as CH₂Cl₂, dimethylformamide (DMF), and toluene. X-ray single crystal analysis was performed to gain deep insight into their molecular packing modes, and single crystals were successfully cultivated by using mixed solvents (CH₂Cl₂ and C₂H₅OH) at room temperature. As shown in Fig. 1b, the crystal structures of these four emitters confirm that these monomers exhibit non-planar and asymmetric geometry with highly twisted donor-acceptor dihedral angles (55.44–83.99°). It is thus inferred that multiple weak forces in the monomers (e.g., C–H···N and C–H··· π) increase the molecular rigidity and reduce the non-radiative decay by impeding the intramolecular vibrational relaxation. Their dimers are arranged in two or three modes through some short contacts of C–H···H, C–H···N and C–H··· π (Fig. 2 and Fig. S10 (ESI†)). Moreover, the crystal packing patterns show a three-dimensional (3D) head-to-tail structure with π ··· π stacking on two donor units from different monomers. However, the introduction of two *t*-butyl segments around these molecules greatly increases the steric hindrance, and thus the molecular packing is not close due to the large intermolecular distances. Therefore, it is expected that the exciton quenching in the aggregated state can be sharply suppressed because of the gaps between the unit cells.

Furthermore, these four emitters show good thermal stability, and the decomposition temperatures (T_d) are determined to be 425 °C, 428 °C, 479 °C, 499 °C for **2Cz2tCzBn**, **2tCz2CzBn**, **2PhCz2tCzBn**, and **2tCz2PhCzBn** (Table 1), respectively, according to the thermogravimetric analysis (TGA) shown in Fig. S11a (ESI†). However, glass transition temperatures (T_g) were not observed for these emitters under the differential scanning calorimetry (DSC) measurements as shown in Fig. S11b (ESI†).

2.2. Photophysical properties

Fig. 3a depicts the absorption and photoluminescence (PL) spectra of four emitters in dilute toluene solution and in neat films. Obviously, all the emitters show broad absorption bands at 370–450 nm, which are assigned as the intramolecular

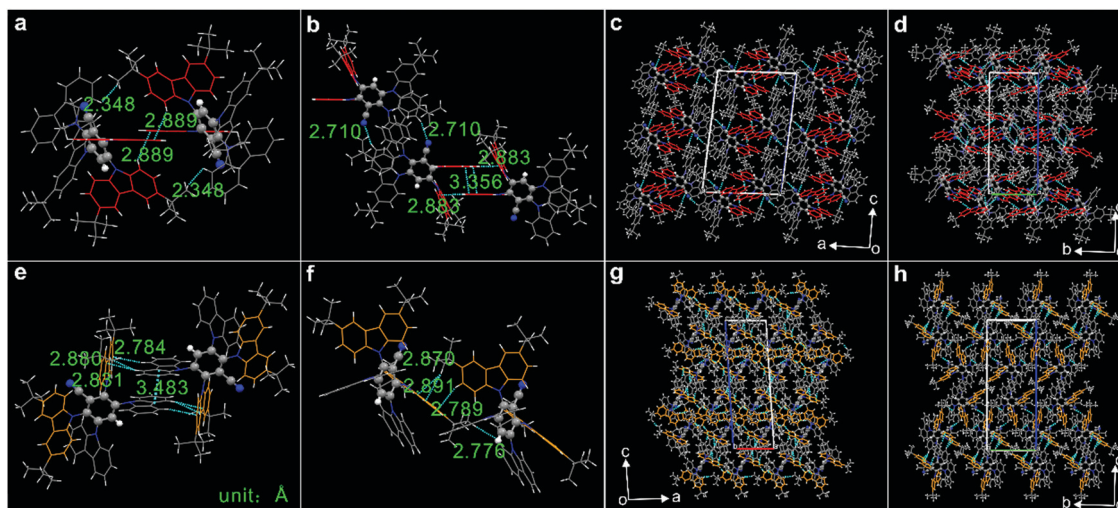


Fig. 2 Single-crystal structures and molecular packing with selected intermolecular distances of (a)–(d) **2tCz2CzBn** and (e)–(h) **2Cz2tCzBn**.

Table 1 Photophysical and thermal properties of **2Cz2tCzBn**, **2tCz2CzBn**, **2PhCz2tCzBn**, and **2tCz2PhCzBn**

	2Cz2tCzBn	2tCz2CzBn	2PhCz2tCzBn	2tCz2PhCzBn
λ_{PL}^a [nm]	488	472	480	483
ΔE_{ST}^b [eV]	0.13	0.13	0.14	0.15
PLQY ^c [%]	78	66	55	53
τ_{p} [ns]	26	10	16	16
τ_{d} [μ s]	3.9	15.7	5.7	5.6
HOMO ^d [eV]	−5.67	−5.65	−5.71	−5.61
LUMO ^e [eV]	−2.85	−2.80	−2.96	−2.86
T_{d}^f [°C]	425	428	479	499

^a Peak wavelength of fluorescence spectra in neat films. ^b Calculated from the onsets of fluorescence and phosphorescence spectra. ^c PLQY of neat films under excitation at 330 nm. ^d Determined from the onset of the oxidation potential in CV measurements, HOMO = (E_{ox} + 4.8 − 0.43) eV. ^e Determined from HOMO and optical gap (E_{g}) by LUMO = HOMO + E_{g} . ^f 5% weight loss of TGA curve.

charge transfer (ICT) transitions from their donors to benzonitrile acceptors. The room-temperature fluorescent spectra of **2Cz2tCzBn**, **2tCz2CzBn**, **2PhCz2tCzBn**, and **2tCz2PhCzBn** in neat films exhibit sky-blue emission with maximum peaks at 488, 472, 480, and 483 nm, respectively (Table 1). A red-shift of 16 nm is observed for **2Cz2tCzBn** relative to **2tCz2CzBn** (Fig. 3a). As the PL spectra of both **2Cz2tCzBn** and **2tCz2CzBn** in toluene solution are basically the same, it is speculated that the difference in PL red-shifts of their neat films arises from the changed molecular stacking. The stronger intermolecular interaction has a larger influence on the optical properties of **2Cz2tCzBn** in neat films as compared to the other molecules (Fig. 2).^{33,34} Low-temperature phosphorescent spectra (taken at 77 K) of four emitters show double peaks with a slight red-shift relative to their room-temperature fluorescent spectra (Fig. 3a). The ΔE_{ST} values for these emitters are calculated to be 0.13–0.15 eV from the difference in onset energies of fluorescence and phosphorescence spectra (Fig. S12 (ESI[†])), which are small enough for potentially efficient RISC and TADF properties. And,

these emitters show solvation effects in different solvents with significant ICT characteristics (Fig. S13 (ESI[†])). The HOMO levels of four emitters were determined from the onset of the oxidation potentials by cyclic voltammetry in CH_2Cl_2 solutions (Fig. S14 (ESI[†])), and the LUMO levels were calculated by taking into account the optical bandgap (E_{g}) from the absorption spectra as shown in Fig. 3a. As listed in Table 1, all the four emitters possess the similar HOMO and LUMO values.

To further assess the photophysical properties in these four emitters in more detail, the temperature-dependent transient PL decay characteristics were also measured in neat films from 100 K to 293 K. As presented in Fig. 3b, the decay curves of the four emitters at room temperature show two distinct periods with a prompt nanosecond-scale lifetime (τ_{p}) and a delayed microsecond-scale lifetime (τ_{d}). As shown in Fig. S15 (ESI[†]), time-resolved spectroscopies at two time-scales exhibit almost identical prompt fluorescence and delayed fluorescence emissions, and the relative intensity of the delayed component increases with respect to the increase in temperature. These characters are consistent with the nature of TADF emissions, indicating the exciton recombination occurring from T_1 to S_1 via an RISC process and then to the ground state (S_0). The decay curves in Fig. 3b are fitted with a biexponential decay function, and the detailed rate constants are summarized in Table 1 and Table S1 (ESI[†]), including τ_{p} , τ_{d} , the radiative decay rate constant (k_{r}), the intersystem crossing rate constant (k_{ISC}), and the RISC rate constant (k_{RISC}). It is noteworthy that the four emitters exhibit faster k_{RISC} than k_{ISC} , revealing the efficient conversion from triplet excitons to singlet excitons through RISC for the delayed fluorescence. Moreover, the **2tCz2CzBn** emitter exhibits the fastest k_{RISC} , which may be helpful for suppressing the ACQ in the films.

In addition, the locally excited triplet states (^3LE) of different donor units in these emitters were examined according to the low-temperature phosphorescence spectra of carbazole (Cz), 3,6-ditertbutyl-Cz (tCz), and 3,6-diphenyl-Cz (PhCz) as shown in Fig. S16 (ESI[†]). It is experimentally evident that the ^3LE energies of tCz and PhCz are lower than that of Cz, indicating

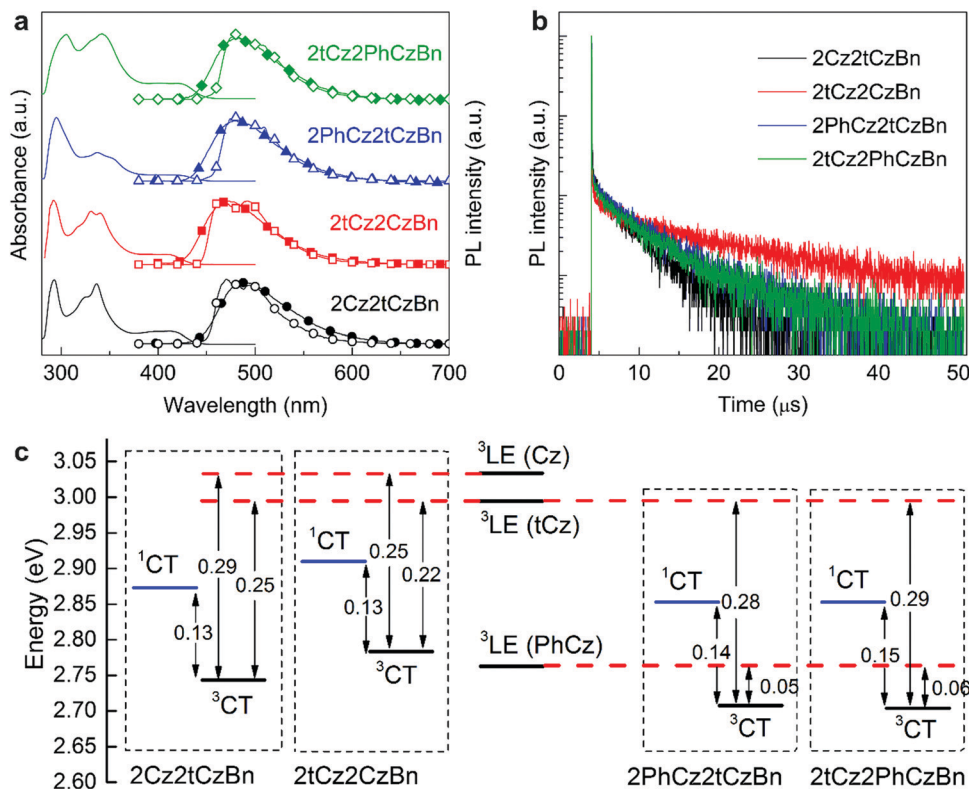


Fig. 3 (a) Steady-state absorption (line) and phosphorescence (77 K, empty symbols) in toluene, and room-temperature fluorescence (solid symbols) in neat films for the four emitters. (b) Transient PL decay curves of the four emitters in neat films at room temperature. (c) Energy level diagrams of the four emitters. The dashed red lines indicate the corresponding ³LE state for reference.

that the combination of two types of donor units in TADF emitters can effectively control the ³LE states and thus the energy level alignment of ³LE, singlet charge-transfer state (¹CT), and triplet charge-transfer state (³CT) (Fig. 3c).

Quantum chemical calculations were carried out to evaluate the electronic states by using time-dependent density functional theory (TD-DFT). As shown in Fig. S17 (ESI[†]), the HOMOs are distributed over all four surrounding donors with slight extensions to the benzonitrile acceptor, while the LUMOs are entirely localized on the benzonitrile acceptor. Accordingly, the almost total separation of HOMOs and LUMOs in these four emitters is expected to allow a small ΔE_{ST} value, which is verified by the experimental measurements (Table 1). Moreover, these four emitters are expected to have high PLQYs due to their high oscillator strength (f) values (0.1254, 0.1008, 0.1459, and 0.1514 for 2Cz2tCzBn, 2tCz2CzBn, 2PhCz2tCzBn, and 2tCz2PhCzBn, respectively) for the transitions between S_0 and S_1 , which were confirmed by the high PLQYs from 53% to 78% of four emitters in the neat films (Table 1). The natural transition orbital (NTO) calculations were carried out for obtaining the hole and particle densities, in which the density distributions of holes and electrons in the excited states were calculated. It is found that the partial overlap between hole and particle densities on the central phenyl ring occurs at the optimized S_1 state (Fig. S18–S21 (ESI[†])), revealing ¹CT is the CT dominant hybrid local-CT excited state (HLCT). Moreover,

the low-temperature phosphorescence spectra of these molecules show double peaks (Fig. 3a), and the hole and particle densities of low-lying triplet state (T_1) and high-lying triplet state (T_2) partially overlap on the central phenyl ring. Therefore, the T_1 and T_2 states are assigned as HLCT excited states for these emitters.^{35,36}

2.3. Device performance

The emission properties of these four emitters in electroluminescent (EL) devices as a function of the doping concentrations were investigated. It is obvious in Fig. S22 (ESI[†]) that the concentration quenching in OLEDs at high doping concentrations can be effectively suppressed, and the EQEs remain nearly unchanged as the doping concentration varies from 10 wt% to 100 wt%. These results indicate that the excitons can be well confined within the emission layer to generate light. The reduced self-quenching for these emitters at high doping concentrations is ascribed to the non-planar structures with highly twisted moieties and the presence of *tert*-butyl groups, which not only limit the intramolecular vibrational relaxation in neat films, but also inhibit the intermolecular π – π stacking.³⁷

Considering the good solution processability and neglectable concentration quenching of these emitters, solution-processed non-doped OLEDs were fabricated by using their neat films as an emitting layer (EML). The device structure was composed of ITO/PEDOT:PSS (45 nm)/PVK (15 nm)/EML

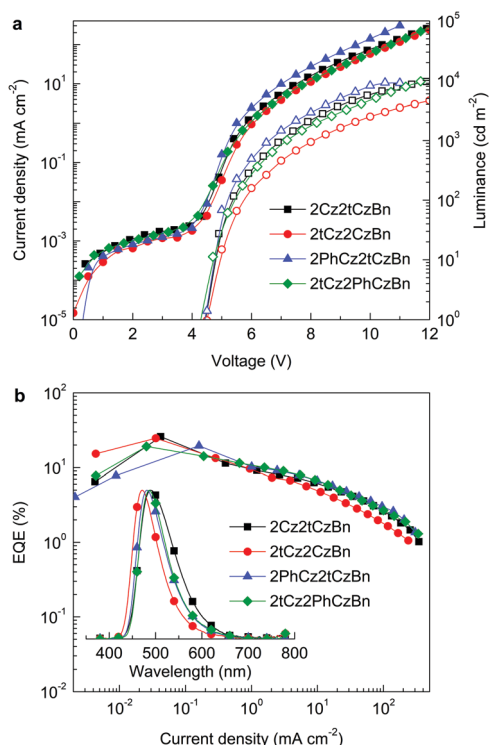


Fig. 4 (a) J - V - L characteristics and (b) EQE versus current density (inset: EL spectra) of solution-processed non-doped OLEDs.

(35 nm)/DPEPO (10 nm)/TmPyPb (40 nm)/LiF (1 nm)/Al (100 nm) (see ESI† for the details of the materials and fabrication process). The atomic force microscopy (AFM) characterization reveals the smooth surface of the solution-processed non-doped EMLs on ITO/PEDOT:PSS/PVK substrates (Fig. S23 (ESI†)), indicating the high quality of these films.

Device characteristics are plotted in Fig. 4, and key performance parameters are summarized in Table 2. As depicted in Fig. 4b, the devices exhibit blue EL emission with the maxima of 488 nm (CIE = 0.21, 0.42), 472 nm (CIE = 0.16, 0.24), 482 nm (CIE = 0.18, 0.35), and 486 nm (CIE = 0.19, 0.38) for **2Cz2tCzBn**, **2tCz2CzBn**, **2PhCz2tCzBn**, and **2tCz2PhCzBn**, respectively, which are almost identical to their PL spectra in neat films (Table 1). Moreover, it is noted that the **2Cz2tCzBn**-based device exhibits a wider EL spectrum than the others, which is consistent with the theory of spontaneous emission that the full width at half maximum is proportional to the square of the peak wavelength. The maximum EQEs of the corresponding devices are 25.8%, 24.5%, 19.5%, and 19.1%, respectively.

Meanwhile, the maximum power efficiency (PE) and current efficiency (CE) are 41.5 lm W⁻¹ and 64.89 cd A⁻¹, 26.3 lm W⁻¹ and 41.9 cd A⁻¹, 26.7 lm W⁻¹ and 42.5 cd A⁻¹, as well as 29.2 lm W⁻¹ and 43.7 cd A⁻¹, respectively (Fig. S24 (ESI†)). The lower device efficiency for **2PhCz2tCzBn** and **2tCz2PhCzBn**-based devices is due to the influence of larger phenyl groups on the periphery of these TADF molecules than that of **2Cz2tCzBn** and **2tCz2CzBn**. The larger phenyl groups on the periphery weaken the role of *t*-butyl at the same time as molecular packing (see Fig. 2 and Fig. S10 (ESI†)), leading to lower PLQYs and EQEs for **2PhCz2tCzBn** and **2tCz2PhCzBn** due to stronger ACQ effects. According to the previous report,³⁸ the high EQEs of these non-doped blue devices might benefit from the outcoupling contribution of horizontal molecular dipole orientation in the aggregated state as observed in Fig. 2 and Fig. S10 (ESI†).³⁸ However, it is found that these molecules have an aggregation-induced emission-enhanced (AIEE) character (Fig. S25 (ESI†)), which might also contribute the high EQEs of these devices. Meanwhile, when comparing with *t*-butyl unsubstituted analogous compounds at low and high concentrations (Scheme S2 and Fig. S26 (ESI†)), the results confirm the effective exciton recombination and largely suppressed ACQ on TADF emitters in the non-doped devices with *t*-butyl substituted TADF emitters. However, the solution process should be further optimized to improve the film morphology to enhance the charge transport and reduce the efficiency roll-off at high luminance as observed in Fig. 4.

Encouraged by the excellent EL performance of these TADF emitters in solution-processed non-doped devices, especially **2tCz2CzBn**, all-TADF white OLEDs were fabricated with a single EML, consisting of ITO/PEDOT:PSS (45 nm)/PVK (15 nm)/**2tCz2CzBn**:0.7 wt% 3DMAC-BP (35 nm)/DPEPO (10 nm)/TmPyPb (40 nm)/LiF (1 nm)/Al (100 nm). Here, 3DMAC-BP is an orange-red TADF emitter previously reported by our group.³² The AFM image in Fig. S27 (ESI†) reveals the low surface roughness for the solution-processed **2tCz2CzBn**:0.7 wt% 3DMAC-BP EML. As shown in Fig. 5 and Table 2, the white device achieves a maximum EQE of 27.3% with a CIE coordinate of (0.34, 0.40), which is one of the highest values of solution-processed white OLEDs (see the comparison of the best reported solution-processed white OLEDs in Table S2, ESI†).^{5,39–42} Meanwhile, as shown in Fig. S28 (ESI†), the EL spectra of the white device remain almost constant at different luminance, indicating the color stability due to the efficient energy transfer from the **2tCz2CzBn** blue host to the orange-red TADF emitter.

Table 2 Performance summary of solution-processed blue OLEDs with non-doped TADF emitters and white OLEDs

Devices	I_{\max}^a [cd m ⁻²]	EQE ^b [%]	PE ^b [lm W ⁻¹]	CE ^b [cd A ⁻¹]	EL ^c [nm]	CIE ^c (x, y)
2Cz2tCzBn	9625	25.8/11.5/7.1	41.5/16.8/8.3	64.8/28.8/18.3	488	(0.21, 0.42)
2tCz2CzBn	4617	24.5/11.9/4.5	26.3/11.6/3.1	41.9/21.0/8.1	472	(0.16, 0.24)
2PhCz2tCzBn	9201	19.5/17.6/7.6	26.7/23.8/8.1	42.5/38.3/16.9	482	(0.18, 0.35)
2tCz2PhCzBn	10 480	19.1/13.2/7.9	29.2/17.9/8.0	43.7/30.4/18.4	486	(0.19, 0.38)
White	4382	27.3/14.7/3.5	35.1/16.4/2.8	67.0/34.3/8.3	—	(0.34, 0.40)

^a Maximum luminance. ^b Maximum efficiency, and values at 100 and 1000 cd m⁻². ^c Recorded at 5 V.

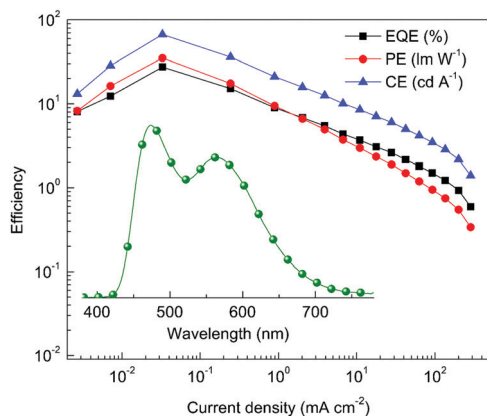


Fig. 5 EL performances of solution-processed white OLEDs. Inset is the EL spectrum operating at 8 V.

3. Conclusions

In summary, two pairs of isomer solution-processable blue TADF emitters have been designed and synthesized, in which the highly twisted hetero-donor configuration with the incorporation of two *tert*-butyl groups in the molecules result in good molecular solubility and efficient TADF characters. The suppressed ACQ of these blue TADF emitters in neat films has been realized due to *t*-butyl-induced inhibition of intermolecular π - π stacking. Solution-processed non-doped blue OLEDs based on these emitters achieve highest EQEs of 25.8%, 24.5%, 19.5%, and 19.1% for **2Cz2tCzBn**, **2tCz2CzBn**, **2PhCz2tCzBn**, and **2tCz2PhCzBn**, respectively. More importantly, high-performance solution-processed white OLEDs are realized by doping an orange-red TADF dopant in the blue TADF emitter for a single-emitting layer, enabling an EQE of 27.3%.

4. Experimental section

4.1. Synthesis of molecules

The synthesis of 3,5-di(9H-carbazol-9-yl)-2,6-bis(3,6-di-*tert*-butyl-9H-carbazol-9-yl)benzonitrile (**2Cz2tCzBn**), 2,6-di(9H-carbazol-9-yl)-3,5-bis(3,6-di-*tert*-butyl-9H-carbazol-9-yl)benzonitrile (**2tCz2CzBn**), 2,6-bis(3,6-di-*tert*-butyl-9H-carbazol-9-yl)-3,5-bis(3,6-diphenyl-9H-carbazol-9-yl)benzonitrile (**2PhCz2tCzBn**) and 3,5-bis(3,6-di-*tert*-butyl-9H-carbazol-9-yl)-2,6-bis(3,6-diphenyl-9H-carbazol-9-yl)benzonitrile (**2tCz2PhCzBn**) was carried out according to a reported method,²⁰ in which the raw material carbazole or 3,6-diphenylcarbazole was replaced with 3,6-ditertbutylcarbazole. After being purified by column chromatography, four compounds were recrystallized with a mixed solvent of DCM and ethanol. Cultivated single crystals were obtained successfully using mixed solvents (CH_2Cl_2 and $\text{C}_2\text{H}_5\text{OH}$) at room temperature. The chemical structures were determined by ^1H and ^{13}C nuclear magnetic resonance (NMR) spectra with Bruker AVANCE III type NMR Spectrometer in CDCl_3 solution, and mass spectra on an Agilent 1260-6125 (atmospheric-pressure chemical ionization (APCI) mode) (see Fig. S1–S9, ESI†).

4.2. Characterization of photophysical properties

UV-vis absorption spectra were measured by a UV-vis spectrophotometer (PerkinElmer Lambda 750) and photoluminescence (PL) spectra were measured by a FM-4 type fluorescence spectrophotometer (JY company, French). Low-temperature phosphorescence spectra were measured with a FLS 920 spectrometer (Edinburgh Corporation) in toluene at 77 K. Photoluminescence quantum yields (PLQYs) for the films were measured using an absolute PLQY spectrometer (C9920-02G, Hamamatsu Photonics, Japan) at room temperature under nitrogen atmosphere. Temperature-dependent transient PL decay measurements were conducted using a Quantaurus-Tau fluorescence lifetime spectrometer (C11367-01, Hamamatsu Photonics, Japan) and a cryostat (Oxford Instruments) with an excitation wavelength of 373 nm under a vacuum. Cyclic voltammetry (CV) measurements were conducted on a RST 3100 electrochemical work station. The HOMO levels were determined from the onset of the first oxidation peak, and the LUMO levels was calculated from the optical bandgap (E_g) and HOMO level.

4.3. Characterization of thermal properties

Thermal gravimetric analysis (TGA) was carried out with a HCT-2 instrument at a heating rate of $10\text{ }^\circ\text{C min}^{-1}$ under a nitrogen atmosphere. Differential scanning calorimetry (DSC) analysis was performed on a Pyris Diamond DSC Thermal Analyzer under a nitrogen flow at a heating rate of $10\text{ }^\circ\text{C min}^{-1}$. All substances show excellent thermal decomposition temperature (T_d , 5% weight loss) from TGA curves. However, the glass transition temperature (T_g) for each compound was not observed from the DSC measurements.

4.4. Device fabrication and measurements

The OLEDs were fabricated on the patterned indium-tin-oxide (ITO)-coated glass substrates with a sheet resistance of $\sim 15\text{ }\Omega$ per square, which were composed of ITO/PEDOT:PSS (45 nm)/PVK (15 nm)/EML (35 nm)/DPEPO (10 nm)/TmPyPb (40 nm)/LiF (1 nm)/Al (100 nm). The indium-tin-oxide (ITO)-coated glass substrates were successively cleaned in an ultrasonic bath with acetone, ethanol, and deionized water, and then dried in an oven at $110\text{ }^\circ\text{C}$. After the UV-ozone treatment for 30 min, poly(3,4-ethylene dioxathiophene):polystyrene sulfonic acid (PEDOT:PSS) (Clevios P VP.AI 4083, Hereus) was spin-coated on the cleaned ITO substrates at 4000 rpm for 40 s and baked at $150\text{ }^\circ\text{C}$ for 15 min. Then, the samples were transferred into a nitrogen-filled glovebox for the spin-coating of the top layers. Polyvinylcarbazole (PVK) (M.W. 136 600, M.N. 56 400) was spin-coated at 2000 rpm for 30 s from 10 mg mL^{-1} 1,2-dichlorobenzene solution onto PEDOT:PSS and baked at $120\text{ }^\circ\text{C}$ for 15 min. The emitting layers (EMLs) were spin-coated onto PVK at 2000 rpm for 30 s from 10 mg mL^{-1} toluene solution, and then baked at $100\text{ }^\circ\text{C}$ for 10 min. Finally, the upper layers of bis[2-(diphenylphosphino)phenyl]-ether oxide (DPEPO), 1,3,5-tri[(3-pyridyl)-phen-3-yl]benzene (TmPyPB), lithium fluoride (LiF) and aluminium (Al) were

thermally deposited on the samples through a shadow mask in the interconnected vacuum deposition chamber at a pressure of $<3 \times 10^{-4}$ Pa. The active areas of OLEDs were defined to be 0.4 cm^2 with overlap between ITO and Al electrodes. After the film depositions, the fabricated devices were transferred to the interconnected nitrogen-filled glovebox for encapsulation with glass caps and epoxy glue. Getter films were also attached to remove oxygen and moisture. Current density–voltage–luminance (J – V – L) characteristics and EL spectra of the devices were measured simultaneously with a source meter (Keithley model 2400) and a luminance meter/spectrometer (PhotoResearch PR670). The CIE 1931 colour coordinates were obtained from the EL spectra. The EQE values were calculated by assuming an ideal Lambertian emission profile.

Conflicts of interest

There are no conflicts to declare.

Acknowledgements

This work is financially supported by the National Key Basic Research and Development Program of China (No. 2016YFB-0401002, 2016YFB0400700), the National Natural Science Foundation of China (No. 61520106012, 61722404, 51873138), the 333 program (No. BRA2019061), Collaborative Innovation Center of Suzhou Nano Science & Technology.

Notes and references

- W. Zeng, T. Zhou, W. Ning, C. Zhong, J. He, S. Gong, G. Xie and C. Yang, *Adv. Mater.*, 2019, **31**, 1901404.
- L. Duan, L. Hou, T.-W. Lee, J. Qiao, D. Zhang, G. Dong, L. Wang and Y. Qiu, *J. Mater. Chem.*, 2010, **20**, 6392.
- T.-H. Han, M.-R. Choi, C.-W. Jeon, Y.-H. Kim, S.-K. Kwon and T.-W. Lee, *Sci. Adv.*, 2016, **2**, e1601428.
- F. K.-W. Kong, M.-C. Tang, Y.-C. Wong, M. Ng, M.-Y. Chan and V. W.-W. Yam, *J. Am. Chem. Soc.*, 2017, **139**, 6351.
- G. Sarada, W. Cho, A. Maheshwaran, V. G. Sree, H.-Y. Park, Y.-S. Gal, M. Song and S.-H. Jin, *Adv. Funct. Mater.*, 2017, **27**, 1701002.
- M.-C. Tang, C.-H. Lee, S.-L. Lai, M. Ng, M.-Y. Chan and V. W.-W. Yam, *J. Am. Chem. Soc.*, 2017, **139**, 9341.
- Y. Wada, S. Kubo and H. Kaji, *Adv. Mater.*, 2018, 1705641.
- H. Uoyama, K. Goushi, K. Shizu, H. Nomura and C. Adachi, *Nature*, 2012, **492**, 234.
- Q. Zhang, B. Li, S. Huang, H. Nomura, H. Tanaka and C. Adachi, *Nat. Photonics*, 2014, **8**, 326.
- S. Hirata, Y. Sakai, K. Masui, H. Tanaka, S. Y. Lee, H. Nomura, N. Nakamura, M. Yasumatsu, H. Nakanotani, Q. Zhang, K. Shizu, H. Miyazaki and C. Adachi, *Nat. Mater.*, 2015, **14**, 330.
- P. Rajamalli, N. Senthilkumar, P. Gandeepan, P. Y. Huang, M. J. Huang, C. Z. Ren-Wu, C. Y. Yang, M. J. Chiu, L. K. Chu, H. W. Lin and C. H. Cheng, *J. Am. Chem. Soc.*, 2016, **138**, 628.
- Z. Yang, Z. Mao, Z. Xie, Y. Zhang, S. Liu, J. Zhao, J. Xu, Z. Chi and M. P. Aldred, *Chem. Soc. Rev.*, 2017, **46**, 915.
- M. Y. Wong and E. Zysman-Colman, *Adv. Mater.*, 2017, **29**, 1605444.
- Y. J. Cho, K. S. Yook and J. Y. Lee, *Adv. Mater.*, 2014, **26**, 6642.
- Y. J. Cho, B. D. Chin, S. K. Jeon and J. Y. Lee, *Adv. Funct. Mater.*, 2015, **25**, 6786.
- Y. Wada, K. Shizu, S. Kubo, K. Suzuki, H. Tanaka, C. Adachi and H. Kaji, *Appl. Phys. Lett.*, 2015, **107**, 183303.
- J. Luo, S. Gong, Y. Gu, T. Chen, Y. Li, C. Zhong, G. Xie and C. Yang, *J. Mater. Chem. C*, 2016, **4**, 2442.
- Y. J. Cho, S. K. Jeon and J. Y. Lee, *Adv. Opt. Mater.*, 2016, **4**, 688.
- G. Xie, X. Li, D. Chen, Z. Wang, X. Cai, D. Chen, Y. Li, K. Liu, Y. Cao and S.-J. Su, *Adv. Mater.*, 2016, **28**, 181.
- S. J. Zou, F. M. Xie, M. Xie, Y. Q. Li, T. Cheng, X. H. Zhang, C. S. Lee and J. X. Tang, *Adv. Sci.*, 2020, **7**, 1902508.
- X. Cai, B. Gao, X.-L. Li, Y. Cao and S.-J. Su, *Adv. Funct. Mater.*, 2016, **26**, 8042.
- J. Lee, N. Aizawa and T. Yasuda, *Chem. Mater.*, 2017, **29**, 8012.
- M. Numata, T. Yasuda and C. Adachi, *Chem. Commun.*, 2015, **51**, 9443.
- Y. Tao, K. Yuan, T. Chen, P. Xu, H. Li, R. Chen, C. Zheng, L. Zhang and W. Huang, *Adv. Mater.*, 2014, **26**, 7931.
- K. Shizu, M. Uejima, H. Nomura, T. Sato, K. Tanaka, H. Kaji and C. Adachi, *Phys. Rev. Appl.*, 2015, **3**, 014001.
- X.-K. Chen, Y. Tsuchiya, Y. Ishikawa, C. Zhong, C. Adachi and J.-L. Brédas, *Adv. Mater.*, 2017, **29**, 1702767.
- J. Lee, N. Aizawa, M. Numata, C. Adachi and T. Yasuda, *Adv. Mater.*, 2017, **29**, 1604856.
- Q. Zhang, D. Tsang, H. Kuwabara, Y. Hatae, B. Li, T. Takahashi, S. Y. Lee, T. Yasuda and C. Adachi, *Adv. Mater.*, 2015, **27**, 2096.
- B. Huang, X. Ban, K. Sun, Z. Ma, Y. Mei, W. Jiang, B. Li and Y. Sun, *Dyes Pigm.*, 2016, **133**, 380.
- D. Zhang, M. Cai, Y. Zhang, D. Zhang and L. Duan, *Mater. Horiz.*, 2016, **3**, 145.
- H. Noda, H. Nakanotani and C. Adachi, *Sci. Adv.*, 2018, **4**, eaao6910.
- F. M. Xie, H. Z. Li, G. L. Dai, Y. Q. Li, T. Cheng, M. Xie, J. X. Tang and X. Zhao, *ACS Appl. Mater. Interfaces*, 2019, **11**, 26144.
- Y. Dong, B. Xu, J. Zhang, X. Tan, L. Wang, J. Chen, H. Lv, S. Wen, B. Li, L. Ye, B. Zou and W. Tian, *Angew. Chem., Int. Ed.*, 2012, **51**, 10782.
- K. Zheng, F. Ni, Z. Chen, C. Zhong and C. Yang, *Angew. Chem., Int. Ed.*, 2020, **59**, 1913210.
- W. Li, Y. Pan, L. Yao, H. Liu, S. Zhang, C. Wang, F. Shen, P. Lu, B. Yang and Y. Ma, *Adv. Opt. Mater.*, 2014, **2**, 892.
- H. Noda, X.-K. Chen, H. Nakanotani, T. Hosokai, M. Miyajima, N. Notsuka, Y. Kashima, J.-L. Brédas and C. Adachi, *Nat. Mater.*, 2019, **18**, 1084.

- 37 X. L. Chen, J. H. Jia, R. Yu, J. Z. Liao, M. X. Yang and C. Z. Lu, *Angew. Chem., Int. Ed.*, 2017, **56**, 15006.
- 38 D. H. Ahn, S. W. Kim, H. Lee, I. J. Ko, D. Karthik, J. Y. Lee and J. H. Kwon, *Nat. Photonics*, 2019, **13**, 540.
- 39 P. S. Ngo, M.-K. Hung, K.-W. Tsai, S. Sharma and S.-A. Chen, *ACS Appl. Mater. Interfaces*, 2019, **11**, 45939.
- 40 C. Li, Y. Xu, Y. Liu, Z. Ren, Y. Ma and S. Yan, *Nano Energy*, 2019, **65**, 104057.
- 41 Y. Liu, X. Wei, Z. Li, J. Liu, R. Wang, X. Hu, P. Wang, T. Qi and Y. Wang, *Adv. Opt. Mater.*, 2018, **6**, 1800978.
- 42 X. Liao, X. Yang, R. Zhang, J. Cheng, J. Li, S. Chen, J. Zhu and L. Li, *J. Mater. Chem. C*, 2017, **5**, 10001.